Earth and Planetary Science Letters, 109 (1992) 431–450 431
Elsevier Science Publishers B.V., Amsterdam

[MK]

Sediment deformation and hydrogeology of the Nankai Trough accretionary prism: Synthesis of shipboard results of ODP Leg 131

A. Taira [a], I. Hill [b], J. Firth [c], U. Berner [d], W. Brückmann [e], T. Byrne [f], T. Chabernaud [g], A. Fisher [c], J.-P. Foucher [h], T. Gamo [a], J. Gieskes [i], R. Hyndman [j], D. Karig [k], M. Kastner [i], Y. Kato [l], S. Lallemant [m], R. Lu [n], A. Maltman [o], G. Moore [p], K. Moran [q], G. Olaffson [r], W. Owens [s], K. Pickering [b], F. Siena [t], E. Taylor [u], M. Underwood [v], C. Wilkinson [g], M. Yamano [w] and J. Zhang [x]

[a] *Ocean Research Institute, University of Tokyo, 1-15-1 Minamidai, Nakano-ku, Tokyo 164, Japan*
[b] *Department of Geology, University of Leicester, University Road, Leicester LE1 7RH, UK*
[c] *Ocean Drilling Program, Texas A&M University, 1000 Discovery Drive, College Station, TX 77845-9547, USA*
[d] *Bundesanstalt für Geowissenschaften und Rohstoffe, Stilleweg 2, D-3000 Hannover 51, FRG*
[e] *Forschungszentrum für Geowissenschaften, GEOMAR, Wischhofstrasse 1-3, D-2300 Kiel 14, FRG*
[f] *Department of Geological Scienes, Brown University, Providence, RI 02912-1846, USA*
[g] *Borehole Research Group, Lamont-Doherty Geological Observatory, Columbia University, Palisades, NY 10964, USA*
[h] *IFREMER / CB, BP 70, 29263 Plouzane, France*
[i] *Scripps Institution of Oceanography, Marine Research Division, University of California, San Diego, La Jolla, CA 92093, USA*
[j] *Institute of Ocean Sciences, Pacific Geoscience Centre, P.O. Box 6000, Sydney, B.C. V8L 4B2, Canada*
[k] *Department of Geological Scienes, Cornell University, Ithaca, NY 14853-1504, USA*
[l] *Hydrographic Department, Maritime Safety Agency, 5-3-1 Tsukiji, Chuo-ku, Tokyo 104, Japan*
[m] *Laboratoire de Géologie, Ecole Normale Supérieure, 24 rue Lhomonde, 75231 Paris Cedex 05, France*
[n] *Department of Geology and Geophysics, University of Minnesota, 310 Pillsbury Drive SE, Minneapolis, MN 55455, USA*
[o] *Institute of Earth Studies, University College of Wales, Aberystwyth, Dyfed SY23 3DB, Wales, UK*
[p] *Hawaii Institute of Geophysics, University of Hawaii, 2525 Correa Road, Honolulu, HI 96822, USA*
[q] *Atlantic Geoscience Centre, Bedford Institute of Oceanography, P.O. Box 1006, Dartmouth, N.S. B2Y 4A2, Canada*
[r] *Department of Geology, University of Stockholm, S-10691 Stockholm, Sweden*
[s] *School of Earth Sciences, University of Birmingham, Edgbaston, Birmingham B15 2TT, UK*
[t] *Istituto di Mineralogia, Università degli Studi di Ferrara, Via Ercole I d'Este 32, 44100 Ferrara, Italy*
[u] *Woodward-Clyde Consultants, 3440 Bank of California Building, 900 4th Avenue, Seattle, WA 98164, USA*
[v] *Department of Geology, University of Missouri, Columbia, MO 65211, USA*
[w] *Earthquake Research Institute, University of Tokyo, 1-1-1 Yayoi, Bunkyo-ku, Tokyo 113, Japan*
[x] *Department of Earth and Space Sciences, State University of New York, Stony Brook, NY 11794-2100, USA*

Received May 28, 1991; revision accepted December 6, 1991

ABSTRACT

The main objective of Leg 131 was to provide data on the deformational processes and associated hydrogeology of the Nankai prism toe. Drilling succeeded, for the first time in the history of ocean drilling, in penetrating the complete sedimentary sequence to basaltic basement, reaching 1327 mbsf (metres below seafloor) with good core recovery (55%). Excellent correlation of the lithology and structure, including the frontal thrust and the decollement, with seismic reflection images was also determined.

Bedding dips, faults and shear bands analyzed in the cores confirm the pattern of deformation to be mainly due to NW–SE shortening, as expected from the plate tectonic convergence vector. Below the decollement, no significant deformation features were observed, indicating that the decollement is a sharp discontinuity in stress transmission.

Correspondence to: A. Taira, Ocean Research Institute, University of Tokyo, 1-15-1 Minamidai, Nakano-ku, Tokyo 164, Japan.

Physical properties data show major discontinuities at the decollement, notably an increase in porosity below the latter. This may indicate excess pore pressure in the subducted section and decollement zone. A less marked increase in porosity below the frontal thrust may reflect the youthfulness of this feature. Attempts to make downhole measurements were severely hampered by unstable hole conditions, but useful constraints have been placed on the thermal regime, and some calibration of laboratory physical properties to *in-situ* conditions has been provided, and *in-situ* stress and pore pressure were measured in the uppermost sediments.

Evidence of channelized fluid flows is inconclusive. No sharp geochemical signatures or unequivocal geochemical anomalies indicative of channelized fluid flow were found. Thermal measurements are not significantly different from those predicted by a purely conductive heat flow model. A signature of low chloride pore water near the decollement may partly be related to smectite diagenesis but may also be due to episodic fluid flow events. We conclude that dewatering probably occurred dominantly through diffuse flow throughout the accreted sediments at this site.

1. Introduction

The accretion of sediments at ocean trenches is an initial step in the process of mountain building and continental crustal growth. An understanding of the processes operating during accretion is thus of fundamental importance. These processes are an attractive target for drilling, which allows both recovery of samples from depth, and *in-situ* measurements of physical parameters.

ODP Leg 110 investigated a clay-dominated prism [1], while in contrast Leg 131 targeted a clastic-dominated prism. The Nankai Trough is considered to be one of the best places to achieve such objectives because: (1) substantial site survey data exist, including excellent images of the thrust structures from seismic profiling [2,3,4,5] and well-constrained velocity structures from two-ship seismic experiments [6], (2) the decollement (detachment zone) is relatively shallow (ca. 1000 mbsf) and can be penetrated with present drilling technology, (3) the trench sediments are sandy turbidites, which represent a type example of the most ancient accretionary prisms (e.g. Shimanto Belt, [7]; Southern Uplands of Scotland, [8]), and (4) an almost direct ancient analogue is exposed on land (Shimanto accretionary prism), providing an opportunity for comparative study.

2. Geological background

2.1. Tectonic setting

The arc–trench system of Southwest Japan shows unique characteristics, which can be sum-

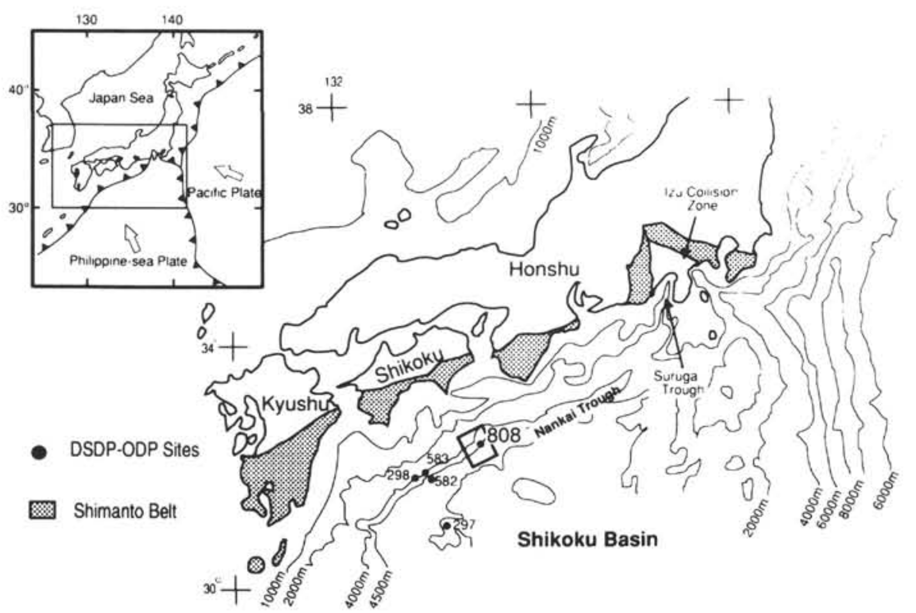

Fig. 1. Location map showing the Nankai Trough and Site 808. The map in the upper left corner shows the Japanese subduction zones and the area shown on the main map. The main location map shows Site 808 and other previous DSDP drilling sites. Stippled area indicates the distribution of the Shimanto Belt (Cretaceous and Tertiary accretionary prism). Box is the area shown in Fig. 2.

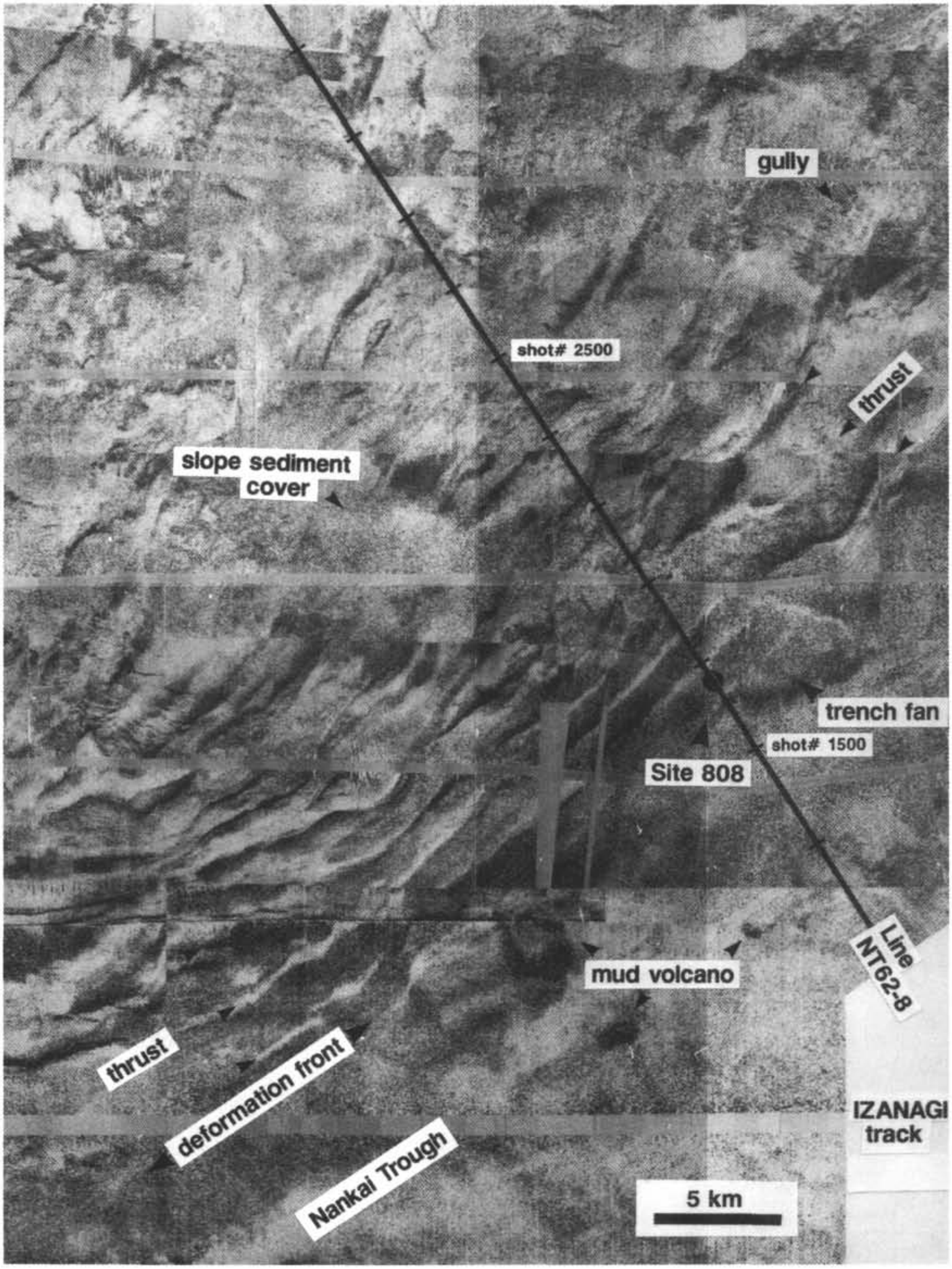

Fig. 2. Backscattering intensity mosaic obtained by 11/12 kHz IZANAGI seafloor imaging system with interpreted geological features. Grey horizontal lines are the shiptracks and the sidescan swath width is 10 km. Seismic profile line NT62-8 is shown with shotpoint numbers. Location of Site 808 is shown by large dot.

marized as follows [see summaries in 9–11]:

(1) The Wadati–Benioff zone extends only to a depth of 50 km.

(2) Scarce volcanic activity since the Middle Miocene.

(3) Localised heat flow values in the trench which are anomalously high compared to the regional background [12].

(4) The trench (Nankai Trough) is shallow and rarely exceeds 4900 m in depth.

(5) The entire arc basement and forearc region are composed of ancient accretionary prisms.

The first two characteristics are closely related to the age and history of the subducted oceanic lithosphere, that of the young, backarc, Shikoku Basin (Fig. 1). The third implies localised fluid flow activity. The fourth and fifth characteristics reflect the long history of large sediment input and accretion at the trench.

The geology of the Japanese Islands shows successive accretionary complexes from the late Palaeozoic to the present day [11]. The youngest accretionary complex, the Shimanto Belt, extends to the Early Miocene. The Shikoku Basin formed by backarc spreading over the period 25 to 15 Ma [13–15]. The opening of the Sea of Japan and subsequent subduction of the Shikoku Basin and the collision of the Izu–Bonin arc have controlled the later tectonic history and sedimentation in the Nankai Trough [11].

In the newly formed Shikoku Basin, fine-grained terrigenous sediments, volcanic ash and biogenic components started to accumulate as hemipelagic sediment cover [16]. The collision of the Izu–Bonin arc against the Honshu arc (called the Izu collision zone) produced major crustal imbrication [17,18]. The topographic manifestation of this tectonic activity is the uplift of the central mountain range of Honshu, which was a main provenance of clastic sediments to the Nankai Trough. An enormous yield of eroded clastics produced a fan–delta system at the collision boundary. Earthquakes periodically destabilized the fan–delta slope, creating turbidity currents which followed westward along the Nankai Trough axis [19]. A sequence of hemipelagite and turbidite sediments has been deformed and scraped off to form an accretionary prism with a typical fold–thrust belt geometry.

2.2. Morphotectonic features of the Nankai Trough

The detailed topography and tectonic regime of the Nankai Trough forearc and trench floor varies considerably along strike. The eastern end of Nankai Trough and its extension, the Suruga Trough, are dominated by the tectonics of the Izu collision zone (Fig. 1).

Toward the west the trough floor becomes flat and a systematic pattern of thrust–fold geometry of the accretionary prism starts to develop along the lower part of the landward slope (Fig. 2). The western end of the Nankai Trough is another collision/subduction boundary, where the Kyushu–Palau Ridge subducts underneath Kyushu Island. The relative convergence vector is approximately normal to the strike of the trough, with a convergence rate of about $\leqslant 30$ mm/yr [20,21].

The structure of the toe of the Nankai Trough accretionary prism in the central and western Nankai Trough (west of 137°E) is characterized by two structural zones, the proto-thrust zone and the imbricate thrust zone [5]. The proto-thrust zone is observed both on the bathymetric map and seismic profiles and is characterized by development of small-displacement (5–20 m) faults, gentle seaward tilting of the trench wedge and gradual thickening of the sedimentary section. Landward, the proto-thrust zone is followed by development of a major thrust (the frontal thrust), which usually has vertical displacements of 50–200 m and which marks the initiation of the imbricate thrust zone. In most seismic sections, the first two or three thrusts are imaged by a reflection and are accompanied by a hangingwall anticline. The thrusts sole out at a decollement in the middle of the hemipelagic section (Fig. 3). At the decollement, the reflected seismic wavelet is of reverse polarity; a low-velocity zone occurs beneath the decollement [22]. Toward the arc, seismic definition is lost and replaced by vague landward dipping reflectors. It is notable, however, that a strong BSR (bottom-simulating reflector) starts to develop slightly landward of the frontal thrust. This BSR has been interpreted as the base of the gas-hydrate stability field, which is an indicator of regional heat flow [23] and possibly fluid flow [24]. Further landward, the accretionary prism is

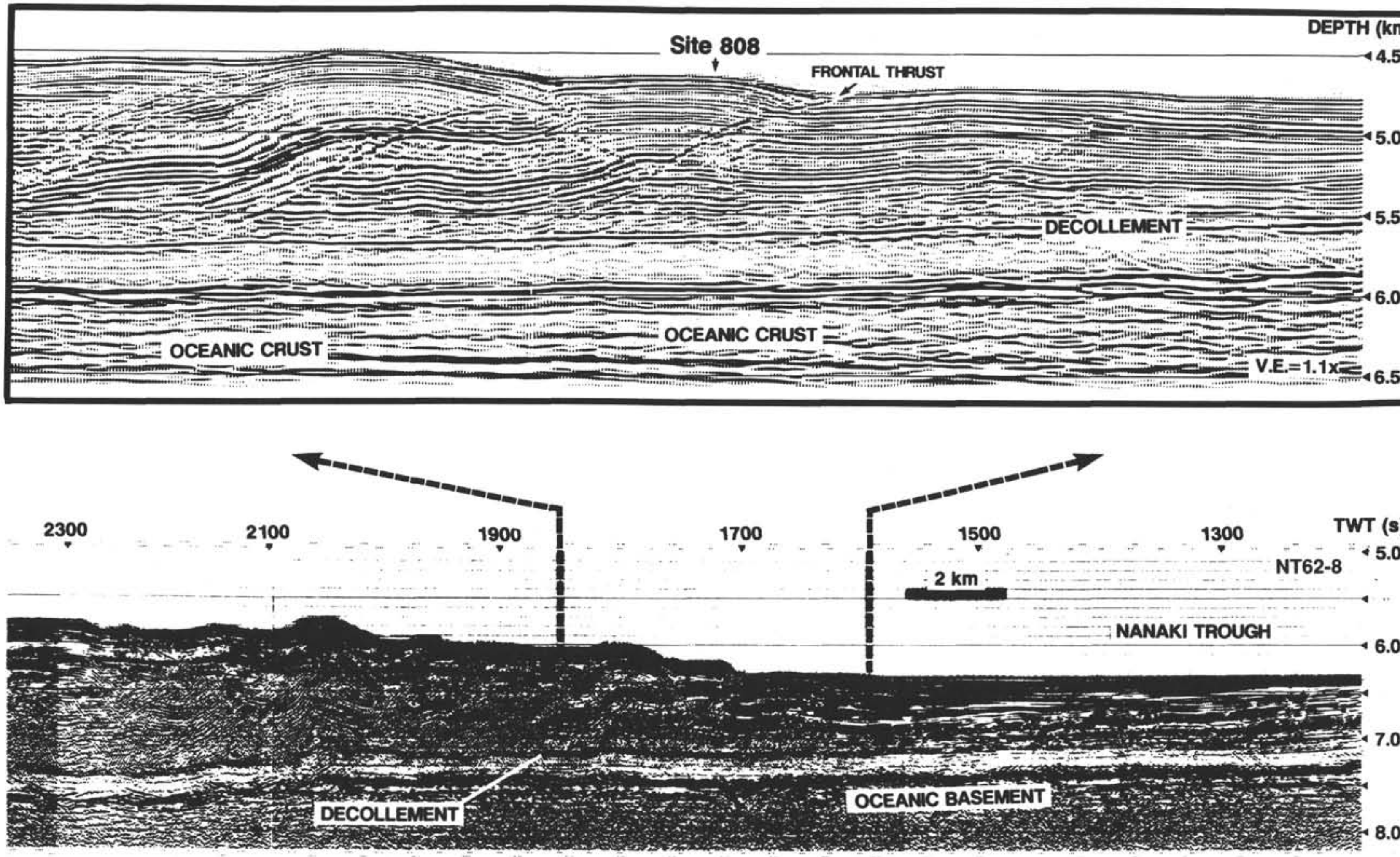

Fig. 3. Seismic reflection profile NT62-8 and location of Site 808. The lower profile is the time-migrated section. TWT (s) indicates two-way travel time in seconds; shotpoint numbers shown on the horizontal. The upper enlarged profile is the depth-migrated section.

covered by a series of slope basins, which are gradually tilted landward and eventually are folded into a synclinorium form.

Previous drilling in this area was carried out on DSDP Legs 31 [25] and 87 [26]. Drilling investigated the undeformed sediments seaward of the deformation front and the prism toe itself, but failed to fully penetrate the toe and intersect the decollement zone.

Although there is gross uniformity in the structural styles of the central and western Nankai accretionary prism, as explained above, there are noticeable local variations. The Leg 131 region shows features that make it well suited to provide an understanding of the structural and hydrogeological characteristics of the accretionary prism, including the following:

(1) The lowest critical taper angle in the Nankai accretionary prism.

(2) The longest seismically traceable decollement development beneath the Nankai prism.

(3) The highest regional heat flow.

(4) One of the thinnest sedimentary sections.

(5) Thrusts and folds with spacing regularity and strike direction continuity that are well documented through the study of Sea Beam bathymetry and sidescan sonar images (Fig. 2).

(6) Oceanic basement near the site is flat and no major disturbance is evident from the seismic profiles.

This site offered an ideal place for the study of hydrogeology and structural evolution. High heat flow, elevated fluid pressure and a relatively simple structural style were expected.

Seismic line NT62-8 (Fig. 3) provides a basic stratigraphic and structural framework for the drilling site, and is complemented by many other regional seismic lines [2,5].

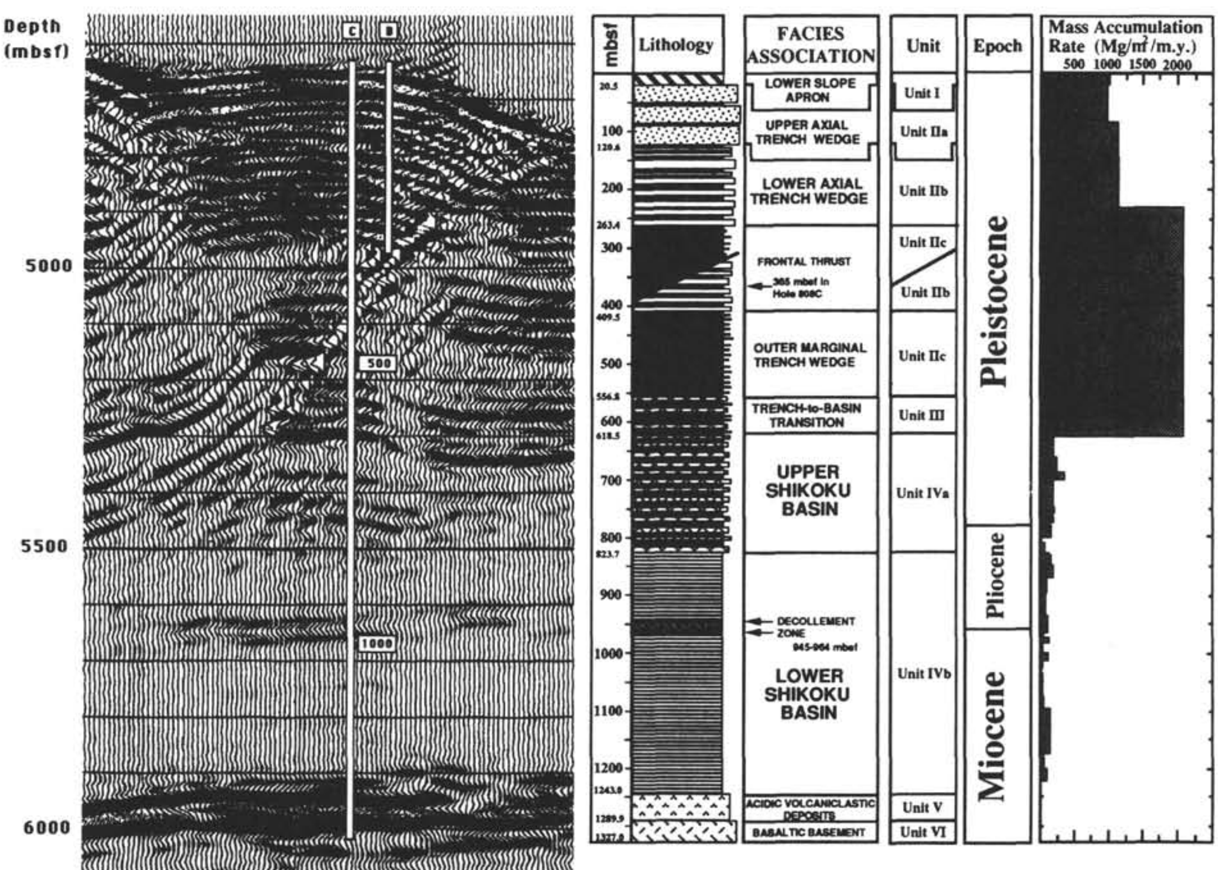

Fig. 4. Location of Hole 808B and 808C on the seismic profile and summary of lithology, facies, unit classification, geological age and mass accumulation rate.

Site 808, the single site of Leg 131, comprised seven closely spaced holes. Holes 808A, B and C were dedicated to coring [27]. The remainder were primarily for downhole measurements and wireline logging. All the holes are within a 150 m × 300 m area and are located towards the oceanward rim of the first hangingwall anticline above the frontal thrust. The deepest penetration, Hole 808C, at 1327 mbsf, is the deepest penetration hole ever drilled in an accretionary prism. The core recovery at Hole 808C was 55%. Although coring was highly successful, unstable hole conditions and mechanical trouble with tools prevented us from carrying out many of the planned downhole measurements. Thus, our description and discussion below will concentrate mainly on the results of core analyses.

3. Lithology and stratigraphy

3.1. Lithologies of Site 808

The lithologies encountered at Site 808 have been divided into five lithological units mainly based on grain size, bed/layer thickness, sedimentary structures and mineralogy, as shown in Fig. 4.

Unit I is about 20 m thick and represents deposits of a trench (landward slope) apron comprising mainly fine-grained turbidite and slump deposits. Some of the thin sandy turbidites may have been deposited by axial flow that lapped onto the lower slope as plumes of suspended sediment. The slump deposits are characterized by repeated occurrence of recumbent folds, bed truncation and pinch and swell features.

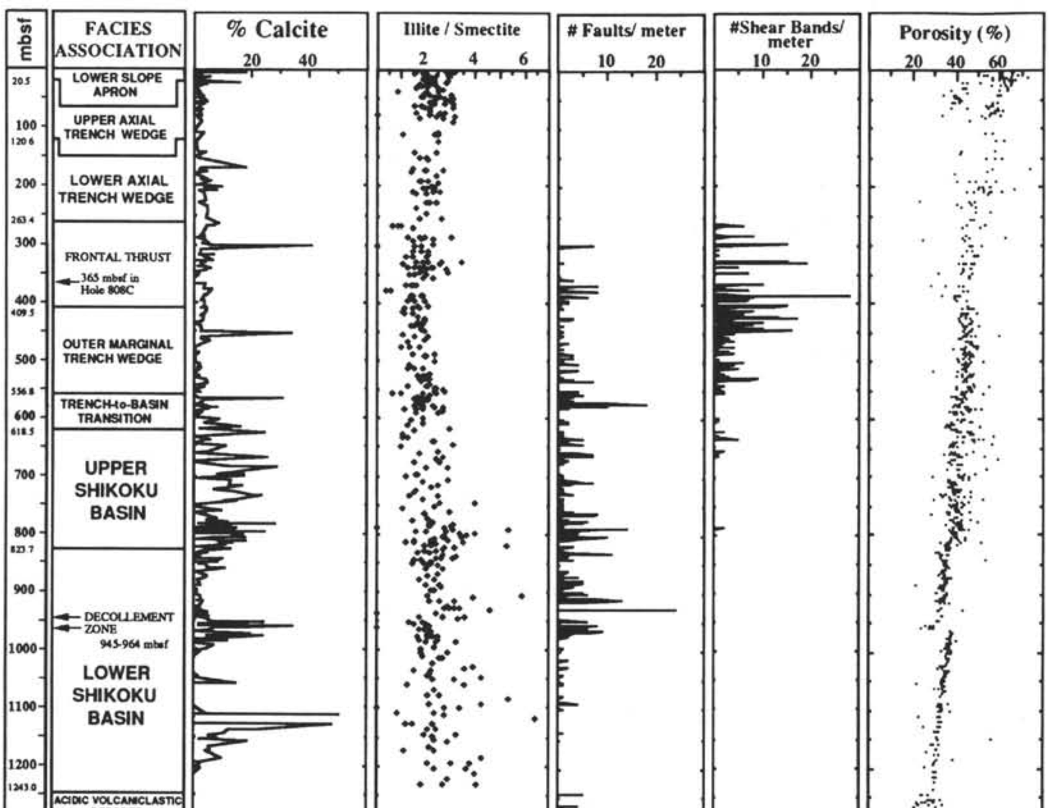

Fig. 5. Figure showing the results of mineralogy (%calcite and illite/smectite determined by XRD analysis), number of small faults and shear bands per metre and porosity at Site 808.

Unit II represents the main episode of trench infilling by turbidites. The unit is divided into three subunits which show an overall coarsening upward trend. Subunit IIa is 100 m thick and composed of thick beds (up to 3 m thick) of very coarse to medium-grained sands showing graded beds, scoured base and concentration of plant debris at the top. This unit is interpreted as axial trench sandy deposits. Subunit IIb is 144 m thick and much finer grained than Subunit IIa. The dominant lithology is 10–50 cm thick turbidite beds composed of fine-grained sand at the base with parallel lamination, ripple lamination and bioturbated silt to thin hemipelagic mud. Subunit IIc, which is 147 m thick, is characterized by very fine grained sand and silt-sized thin turbidite layers intercalated with hemipelagic mud. Subunits IIb and IIc are inferred to represent outer depositional sites of the axial trench environments.

Unit III is 62 m thick and shows intercalations of three different types of lithology: thin graded silt, highly bioturbated hemipelagic mud and volcanic ash layers. Because this unit shows characteristics of both overlying Subunit IIc (silt turbidite) and Subunit IVa (hemipelagite and ash layers), it unit represents a transitional zone like the trenchward slope of the outer swell of an oceanic plate.

Unit IV is dominated by a rather monotonous sequence of bioturbated olive grey hemipelagic mudstone which is divided into two subunits mainly based on the abundance of ash layer intercalations. The volcanic ashes are more frequent in Subunit IVa than IVb.

Unit V shows a unique lithology: thick white acidic tuffs interbedded with variably coloured (greenish grey, buff red and dark olive grey) hemipelagic mudstone, the total thickness of which is 46 m. The maximum thickness of one particular acidic tuff bed reaches 4.5 m; this bed also shows altered glass shards.

Unit VI represents basalts and intercalated red tuffaceous mudstones. The uppermost unit of the basalts is inferred to be a sill intruded into sediments, and the lower part is interpreted to be pillow lavas.

3.2. Mineralogy and diagenesis

Thin section examination of turbidite sands shows a variety of components, including quartz, feldspar, volcanic rock fragments, sedimentary rock fragments, chert and metamorphic (generally low-grade) rock fragments, and several suites of heavy minerals, typically pyroxene, amphibole and mica. The data (see [27] for details) are similar to Taira and Niitsuma's tabulation [19] and support their inference of the Suruga Trough–Fuji River as the drainage source.

The bulk mineralogy determined by XRD analysis indicates the relative proportions of the major crystalline components of the sediments: quartz, feldspar, clay minerals and calcite. Other minor components include several species of heavy minerals and zeolites.

The calcium carbonate content of the sedimentary section (Fig. 5) is primary controlled by the calcareous fossil content. Sporadic occurrence of very high values ($>30\%$) occur where sediments are light olive grey, and this probably represents events of calcareous turbidity current deposition. Discarding these high values, the pattern of $CaCO_3$ content shows three maxima: a broad peak from 600 mbsf to 850 mbsf, a sharp peak at 970 mbsf, and another peak at 1150 mbsf. The first, 600–850 mbsf, peak coincides with the upper Shikoku Basin hemipelagite, where nannoplankton and foraminifera content increases. The second peak matches roughly with the decollement; the maximum extends from within the zone of deformation to 20 m into the undeformed section below. The origin of this $CaCO_3$ content is not clear as there is no visible increase in biogenic component. There is a possibility that this peak of $CaCO_3$ content may reflect diagenetic carbonate precipitation. The third peak seems to be related to another interval of increased biogenic contribution.

In order of relative abundance, clay minerals include illite, chlorite, smectite and kaolinite. These clay minerals were supplied by diverse detrital sources, as suggested previously [28]. The abundance of these minerals relative to total bulk does not change significantly with depth; however, there are subtle changes within the clays that are important. Observations of core lithologies indicate that volcanic input increases in the lower part of the sedimentary section relative to the upper sandy units. However, the data show a small decrease in smectite content relative to illite. It is noteworthy that the X-ray diffraction peak associated with the (001) illite reflection becomes increasingly broad and asymmetric beginning at a depth of roughly 530 mbsf. These lines of evidence indicate that possible diagenetic alteration of smectite to illite may have taken place below about 500 mbsf. Additional detailed work must be carried out, however, before we can make further inferences concerning such important processes.

Another aspect of diagenetic alteration detected was the discrete occurrence of zeolites. Zeolites, mainly clinoptilolite, occur in greatest abundance from 740 to 810 mbsf, which matches

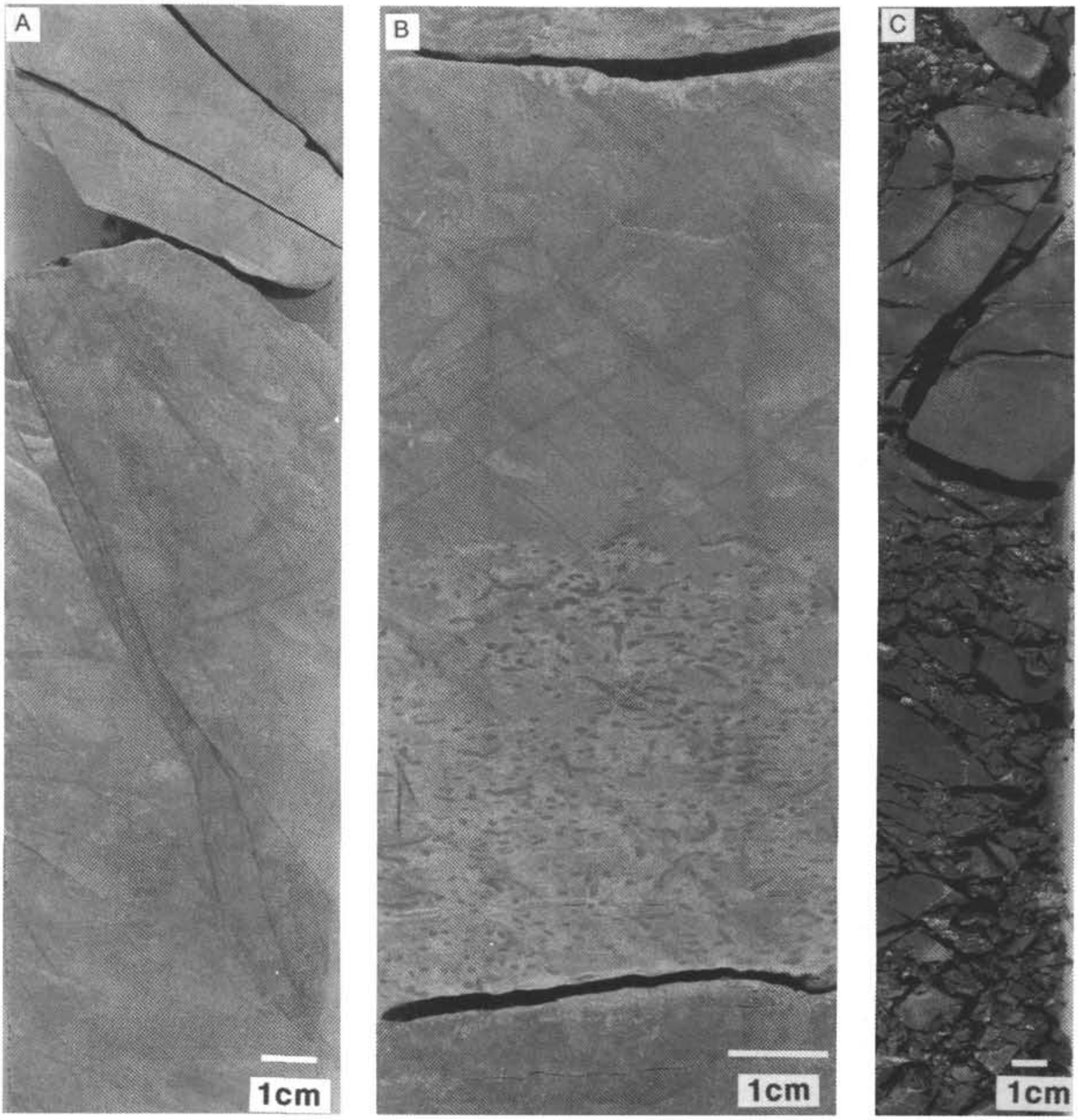

Fig. 6. Core photos of (A) small faults (Hole 808C, centre of photo is 530.7 mbsf), (B) conjugate shear bands (Hole 808C, 444.7 mbsf) and (C) breccias in the decollement (Hole 808C, 959.3 mbsf).

with the lower part of ash-rich Subunit IVa, indicating diagenetic alteration of volcanic ashes below this horizon.

3.3. Biostratigraphy and magnetostratigraphy

The age assignment of the stratigraphic section recovered at Site 808 was achieved mainly by two methods: calcareous nannoplankton biostratigraphy and magnetostratigraphy. Nannoplankton occur throughout the section despite the near lysoclinal depth of deposition. Preservation was moderate to poor, but was adequate for reasonable age control.

The result of palaeomagnetic measurements shows good agreement with biostratigraphy. The intensity of magnetization is generally strong compared with normal marine sediments. The magnetization is stable, but the intensity decreases considerably between 700 to 800 mbsf. Shipboard examination of magnetic properties of discrete core specimens from this interval suggests the possibility of rather strong remagnetization imprints at that interval. A reasonably well constrained magnetostratigraphy was established throughout the section, discarding parts of the interval with very weak intensity.

Figure 4 shows the established chronostratigraphy, age assignment and rate of sedimentation. The base of Unit III, which shows the first influence of the trench turbidity current activity, is 0.46 Ma. The Shikoku Basin hemipelagic sedimentation ranges from 0.46 to 15 Ma. The rate of trench sedimentation reaches almost 2000 $Mg/m^2/m.y.$ (1400 m/m.y.). The Shikoku Basin hemipelagic sequence, Unit IV, shows a rate of sedimentation of about 150–200 $Mg/m^2/m.y.$, an order of magnitude smaller than for the turbidite sequence.

3.4. Correlation with seismic units

Depth migration of seismic line NT62-8 provided an excellent image in depth because of the velocity control provided by a previous two-ship experiment [6]. Thus, there is a good correlation between the lithological units based on core description and the major seismic units defined in the profile (see Fig. 4). The upper part of the axial sandy trench deposits, Subunits IIa and IIb, is represented by a series of laterally continuous, medium-amplitude reflections. The outer marginal trench deposits (Subunit IIc) are a zone of low-amplitude reflections imaged above and below the frontal thrust fault. The trench-to-basin transition (Unit III) is a series of four moderate to high amplitude reflections that are continuous laterally to the southeast below the trench wedge. The upper 60 m of the upper Shikoku Basin hemipelagites (upper part of Subunit IVa) are acoustically nonreflective. The lower part of Subunit IVa is a series of three moderate-amplitude, laterally continuous reflections. The upper part (above the decollement) of the lower Shikoku Basin hemipelagites (Subunit IVb) is characterized by low-amplitude discontinuous reflections. Below the decollement Subunit IVb is almost acoustically nonreflective; this zone has several very low amplitude, highly continuous reflections. The acidic volcaniclastic deposits (Unit V) are represented by a single moderate-amplitude reflection overlying the very high amplitude, laterally continuous, low-frequency basement reflection.

4. Structural geology

4.1. Classification of structures and structural domains

Leg 131 produced probably the largest structural data set in the history of DSDP-ODP Legs, including 3000 structural measurements, over 70% of which have been corrected to geographic coordinates using palaeomagnetic data. The structural features observed at Site 808 were classified into four main types: small faults, shear bands as previously described from Leg 87 cores [29], a zone of breccia and scaly fabrics, and steepened beds.

Small faults (Fig. 6A), which are the most abundant features in the cores, typically occur as narrow (< 1 mm), sharply bounded zones of small displacement (less than a few centimetres) that appear much darker than the surrounding sediments. The fault surface is commonly coated with dark grey material, which XRD analysis indicated to be rich in iron-sulphate minerals (greigite/pyrite). The surfaces show slickenlines and various degrees of polishing.

Shear bands appear macroscopically as diffusely bounded zones that are slightly darker than the surrounding material (Fig. 6B). The bands are commonly a few millimetres across, but some examples reach a width of 1 cm. Although the bands show some displacement it is relatively small (less than a few millimetres) compared with the small faults, even when the bands are very wide and appear well developed. The surface grooves and polish are not as well developed as in the faults. In three dimensions, the bands appear to form relatively simple conjugate sets centred on bedding, with a dihedral angle that ranges from 30 to 45°.

The zones of breccia and scaly fabrics are marked by a high concentration of trapezoidal and lens-shaped fragments of mudstone with highly polished and/or slickensided surfaces (Fig. 6C). In addition, steepened bedding dips occur in

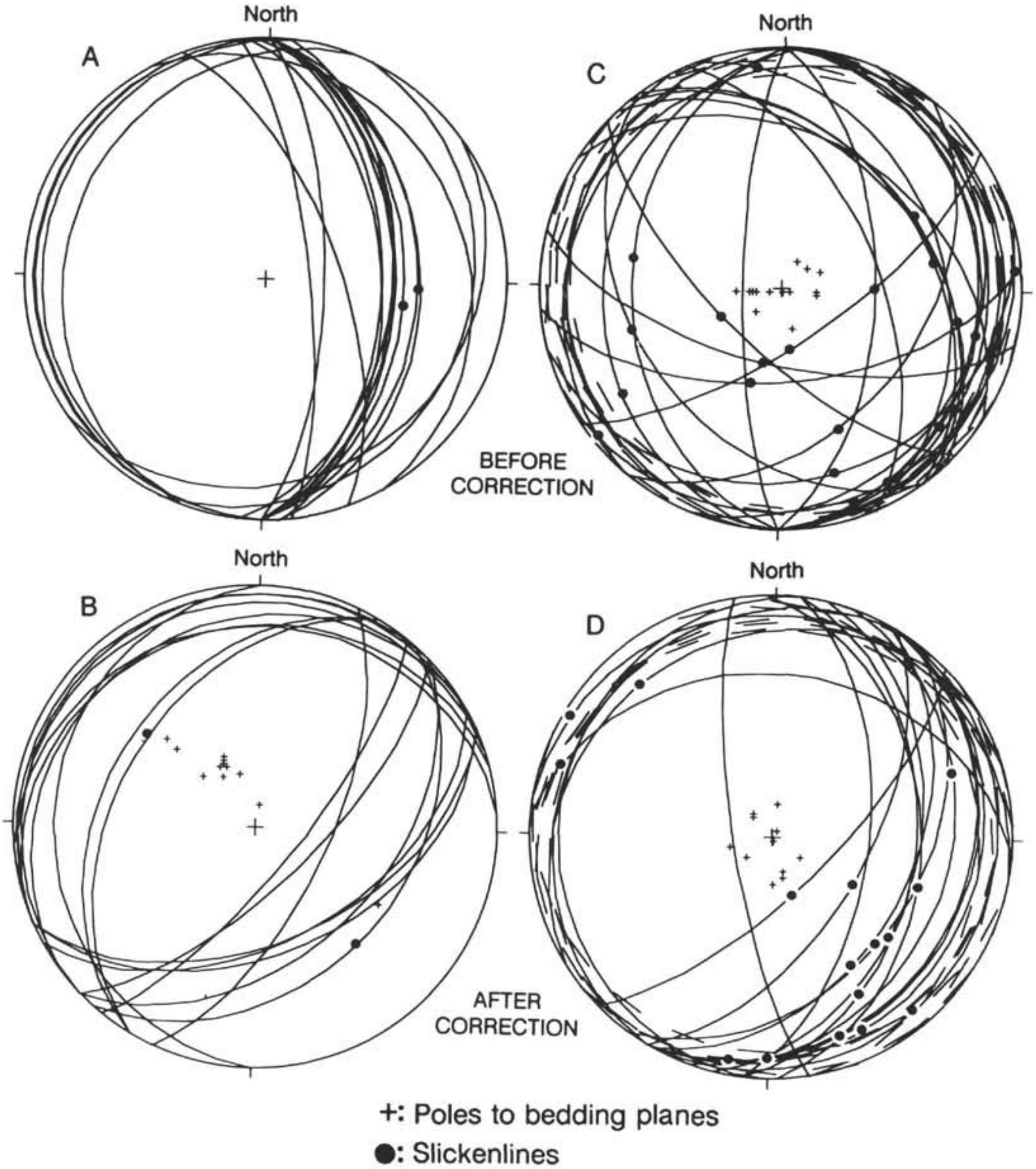

Fig. 7. Stereonet projections of typical structures from Hole 808C. (A) Uncorrected orientations of shear bands and slickenlines (530–539.7 mbsf). (B) The same structures and poles to bedding planes after correction with palaeomagnetic data for rotation due to drilling. (C) Small faults, slickenlines, bedding (dashed line), and poles to bedding planes (568–578.3 mbsf). (D) The same structures after palaeomagnetic correction. These are equal-area lower hemisphere projections.

several horizons, including overturned bedding, which was detected at the frontal thrust.

Observation and measurements of these structural features throughout the core (Fig. 5) enabled six structural domains to be distinguished. Domain 1 represents the shallowest structural level. The upper part of the domain, above 200 mbsf, shows syndepositional deformation features including a 10 m thick slump horizon, and below 260 mbsf tectonic structures become increasingly abundant. Domain 2 includes the interval of intense deformation that constitutes the frontal thrust. This zone is defined by steepened and overturned bedding dips, faulting and the development of fine breccias and scaly fabrics. Domain 3 occurs between the frontal thrust and decollement and is composed of moderately to intensively deformed trench deposits to hemipelagic mudstone of the Shikoku Basin (Units II to IV). The deformation is characterized by arrays of the macroscale deformation features mentioned above, showing a markedly inhomogeneous distribution. Domain 4 includes the interval of intense faulting and brecciation associated with the decollement. Domain 5 represents the interval of relatively undeformed hemipelagic sediments of Unit IV that is being underthrust beneath the decollement and the Nankai accretionary prism. Domain 6 comprises the fractured and veined basalts of the oceanic basement.

In general, the structures strike NE–SW, parallel to the Nankai Trough, when palaeomagnetically corrected for rotations due to drilling. Rotated slickenlines and conjugate shear bands and faults also suggest that the shortening direction associated with these structures (see examples in Fig. 7) trends northwest, parallel to the inferred plate convergence vector. There are a few exceptions to this generalization, which will be discussed below. We discuss here three important structural features of this site in more detail: the frontal thrust, accreted sediments and the decollement.

4.2. *Frontal thrust zone*

This zone corresponds to structural domain 2 and contains the highest concentration of steeply dipping beds. Within this zone, bedding increases in dip up to 90° and becomes overturned. The observed bedding orientations closely constrain the style and orientation of the overall structure within the thrust zone, even though the core recovery was relatively poor in the upper part of this zone. When corrected palaeomagnetically for rotations due to drilling, the bedding planes dominantly face towards the northwest, suggesting the presence of inclined folds, with axial surfaces dipping towards the northwest.

The shear bands and faults range in abundance between 5 and 20 per metre, with localised zones having 20 fault/shear bands per metre as shown in Fig. 5. In general, these structures strike NE–SW when corrected with palaeomagnetic data. The breccia/scaly fabrics are best developed at about 366 mbsf.

The frontal thrust of the prism is therefore regarded, in Hole 808C, as a zone which extends from 360 down to 390 mbsf, based on the distribution of scaly breccias and frequency of faults and shear bands. The displacement associated with the thrust zone is best marked by a mudstone-pebble conglomerate horizon, the top of which is recognised at both 263.4 mbsf in Hole 808B and at 409.1 mbsf in Hole 808C. The observed vertical difference between these two levels, the stratigraphic throw of the thrust, is therefore 145.7 m, and, assuming a 28° dip for the structure, the fault-parallel separation is 309 m. This last value also represents the true total movement within the thrust zone, assuming that the motion is dip-slip as suggested by slickenline orientations.

4.3. *Deformed sediments between the thrust and decollement*

The sediments between the frontal thrust and decollement record the initial deformation of the lower part of the accretionary prism. This is characterized by an overall decrease in the development of shear bands with depth, a generally low bedding dip (< 10°), and the presence of faults throughout the zone but with intervals of marked concentration (Fig. 5). The shear bands are concentrated in the 200 m interval between just above the frontal thrust (above 300–350 mbsf) and 550 mbsf where there are on average over 10 bands per metre. Below about 560 mbsf the shear bands are very scarce and the few bands that do occur are only between 600 and 800 mbsf.

The distribution of shear bands seems to be controlled by two factors, the magnitude of the tectonic strain (associated with the frontal thrust), and the pre-existing sedimentary fissility (perhaps enhanced by compaction) in the fine silts and muds of Subunit IIc.

The orientation of small faults changes down the section (see [27] for details). Above 600 m, the faults are generally conjugate, as are shear bands. Between 600 and 720 m, the faults show a more complex pattern of orientation, generally with low dip angles but variable trends forming specific clusters—reverse faults trending northwest and northeast and normal faults trending N–S. The slickenlines, however, consistently show a NW–SE movement direction. Between 780 and 820 mbsf, there are apparently two sets of fault orientations, one similar to the 600–720 m interval and the other consisting of high-angle normal faults striking NW–SE with down-dip and strike-slip offset. The latter set predates the former and, judging from the paucity of open fractures, seems to represent an early phase of faulting.

Between 880 and 930 mbsf, further complexity occurs. This zone marks the highest concentration of faults, where in addition to the fault types described above a rather peculiar set of faults is recorded. This exotic set shows slickenlines trending east-northeast, parallel to the Nankai Trough and at 90° to the shortening direction inferred for the accreted sediments at higher structural levels. The reason is unclear and requires further careful investigation.

An isolated, centimetre-wide sandstone dyke occurs at 813 mbsf. This is composed of medium-grained sandstone injected into a dark grey claystone host rock. The dyke dips to the northwest, approximately parallel to several faults that are also present in this area. This feature presents the only physical evidence observed in the cores for overpressuring anywhere within the prism. The source of the sand, however, is quite enigmatic, because there are no sand layers encountered below 650 mbsf.

4.4. Decollement

Domain 4 represents the basal decollement of the Nankai accretionary prism. It contains fault densities averaging 5 to 6 per metre compared to the values of 0 to 1 above and below (Fig. 5), and a local increase in bedding dip and marked brecciation. The top of the domain is sharply bounded, marked by the abrupt onset of a well-developed 1.5 m thick breccia/scaly fabric zone at about 945 mbsf and a sharp increase in the number of faults per metre. The bottom of the domain at 964.3 mbsf is also very sharp and is marked by both an abrupt decrease in brecciation and by a rapid drop in the number of faults per metre. We therefore consider this domain to be about 19 m thick.

Within this interval of intense faulting and brecciation we were able to locate a 1–2 m section that was both magnetically and structurally coherent. This zone was carefully analysed for fault orientation and kinematic indicators in order to compare it with the sections above and below the decollement. The faults in this interval generally dip to the northwest and have slickenlines that trend NW–SE, consistent with the plate convergence direction in this area (see [27] for details). No prominent mineralized veins were recognised on initial core description.

In summary, the strain recorded in the accreted sediments above and within the decollement suggests consistent NW–SE shortening, which is parallel to the convergence direction. On the other hand, below the decollement, there is no evidence for such strain and deformational structures are very sparse (see Fig. 5). Close proximity of two separate stress regimes implies that the decollement is a zone of very low strength.

5. Physical properties

The physical properties data at Site 808 were collected at a mean sample spacing of about 1 m. The variability is, however, high. Sampling was restricted in the upper part of the section, above 300 mbsf, where the recovery was poor and the cores were badly disrupted by gas expansion. Below this, core recovery was generally good, except in specific zones which unfortunately coincide with critical structures such as the decollement. Measurements were obtained primarily from Hole 808C, which was cored through the interval from 300 to 1290 mbsf in the sediments. The upper 350 m of the sequence was cored in Holes 808A and 808B. In the following discussion the data have been assembled into one continuous array with depth.

The most striking feature of the physical properties record is a dramatic downhole decrease in bulk density and velocity, and increase in porosity which occurs at the decollement as shown in Fig. 5. When viewed in detail, the zone can be discerned where the density increases sharply by about 0.1 g/cm^3 at 950 mbsf and then decreases equally sharply by about 0.25 g/cm^3 at 965 mbsf. Both above and below it the sediment shows a normal compaction trend with depth, this trend being offset sharply across the decollement. The lithology is uniform across this whole zone, indicating that the effect is tectonic. From comparison with the porosity–depth function of Shikoku Basin deposits from Site 582 [30] it appears most likely that the sediments under the decollement are undercompacted. This in turn suggests restricted dewatering and elevated pore pressures within this zone.

Above about 800 mbsf the scatter in the physical properties data is greater, so that the underlying trends are not so clearly displayed. This scatter results from the increased lithological diversity on a fine scale through the upper Shikoku Basin hemipelagic and ash/tuff (Unit IV) and the transitional and trench wedge turbidite deposits (Units III and II).

Just above 400 mbsf a less distinct offset in the density and velocity data has a similar pattern to that seen at the decollement. This is the signature of the frontal thrust fault. Here it can be seen that the sediment in the footwall of the thrust has not responded to the increased lithostatic load created by the fault displacement. This may be interpreted as indicating delayed dewatering due to the very recent nature of the thrust event.

Thermal conductivity data broadly follow the pattern of the porosity variation, as may be expected, with some moderation by grain compositional effects [27]. Interestingly, there is no ob-

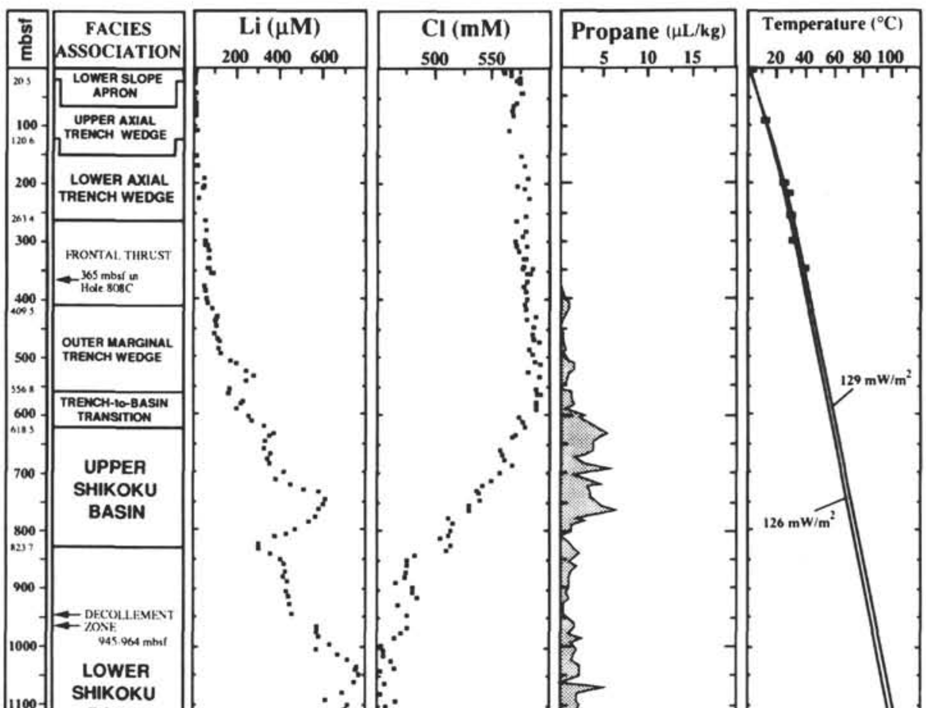

Fig. 8. Figure showing the results of lithium (Li) and chloride (Cl) concentrations in pore water, headspace gas concentrations of propane, and temperature gradient.

servable offset in the thermal conductivity curve at the decollement where the porosity values are offset sharply. The main importance of the conductivity data is that they provide a firm basis for the extrapolation of the observed shallow temperature measurements throughout the sediment column.

6. Geochemistry

6.1. Inorganic geochemistry

Effects observed in the inorganic analysis of pore-water chemistry can be broadly divided into four categories: biogenic effects mainly above 150 mbsf; lithological effects controlled by the varying chemistry of the sedimentary sequence, occurring at many lithological boundaries; diagenetic effects linked to either mineralogical changes or gas-hydrate occurrences, mainly above 250 mbsf; and potential changes in concentration gradients due to fluid flow.

Biogenic effects are clearly evident in the concentration of dissolved sulphate, alkalinity, ammonia and phosphate [27]. Rapid changes in concentrations in the uppermost 20 m are mainly a product of the biological activity in this zone. Below this, biogenic methane production is linked with the changes in alkalinity and sulphate reduction.

Lithological boundaries are associated with signals in many chemical constituents, most distinctly shown in the concentrations of lithium and silica. The sharp variation in the Li, Mg and Ca concentration gradients with no apparent smoothing due to diffusion (see Fig. 8) indicates that the thrust fault is young, probably less than 10,000 years old. This can be taken as evidence for little fluid circulation along the fault zone, which would probably have altered this specific profile.

The boundary between the trench fill turbidites and the trench–basin transitional deposits at 560 mbsf produces major concentration changes in many components. Dissolved silica shows marked variability below this boundary, probably in response to the ash horizons present from this depth down to 820 mbsf [27]. Lithium (see Fig. 8), calcium, magnesium and potassium also have abrupt concentration gradient changes at 560 mbsf, which could be related to diagenetic effects influenced by the lithological change. Below 1200 mbsf the observed changes in calcium and strontium concentration and in the Na/Cl ratio are characteristic of alteration reactions occurring in the volcanogenic sediments overlying the basaltic basement.

A possible diagenetic front may be indicated at 195 mbsf. Here a sudden rise in silica, a local lithium maximum, a calcium increase and a magnesium decrease form a pattern comparable to that seen at other drilling sites [31], which is interpreted as alteration of volcanogenic material. Interestingly, these effects also coincide with the calculated depth of the gas-hydrate dissociation at this site.

Because chloride is a conservative component, fluid flow effects can often be identified from effects on the chloride concentration profile. As shown in Fig. 8, a major chloride anomaly exists as a minimum below the decollement at about 1100 mbsf, reaching 20% dilution of seawater. This anomaly grades upwards to a maximum at 560 mbsf. Although this low chloride concentration profile has some similarities to those found in the decollement zone of the Barbados prism [32] where fluid flow was implied, some of the chloride dilution effect here can be attributed to *in-situ* reaction, particularly clay dehydration at the ambient temperatures of 60–120°C. Estimates of the diffusion effects on the chloride profile indicate that any introduction of a low-chloride fluid along the decollement must have occurred several hundreds of thousands of years ago. Evidence for fluid flow at other depths in the prism is weak or non-existent.

6.2. Organic geochemistry

Despite a general decrease in the organic matter content of the sediment with increasing depth, marine organic matter is nevertheless present throughout. Total organic carbon ranges between 0.7 and 0.2%. Above 600 mbsf the absence of sulphate coupled with methane increases suggests a bacterial origin for that methane (Fig. 8). The gas components ethane to pentane indicate that thermogenic gases appear below 380 mbsf (see Fig. 8 for propane), mixed with biogenic components to 1020 mbsf; below this depth only thermogenic gases are found.

The gas composition indicates that thermogenic gases from 600 to 800 mbsf and 1060 to 1280 mbsf were generated *in situ* from the organic matter of the host sediments. This observation raises several important questions: The maturity of the organic matter appears higher than expected from extrapolated models using heat-flow and temperature data. Also, the almost total absence of organic gases within the zone from 800 to 1060 mbsf remains enigmatic; organic material is definitely present within the sediments. Either maturation temperatures were not reached, or the gases have been removed. The existence of the decollement centrally within this anomalous zone may not be coincidental. However, there is no evidence for gas migration at the decollement level, or at the frontal thrust. Resolution of this problem must await later analysis of (i) the state of maturation of the organic carbon and of (ii) the isotopic composition of the hydrocarbon gases.

7. Downhole measurements

Despite considerable efforts, the logging activities met with very limited success, with recovery of only short sections of open-hole logs and some through-pipe logs; both of these were restricted to the interval from 0 to 750 mbsf. The causes of this were a combination of loose sands, swelling clays and rubbly fault zones, all of which made the holes highly unstable. It is tempting to speculate about the component of hole instability caused by breakouts due to tectonic stress effects, but no direct evidence was gained to indicate this might have been the case.

The open-hole logs cover the depth ranges 80–180 mbsf and 525–615 mbsf. Only in the lower interval was core recovery good. Here the log and laboratory average values for seismic velocity agree very closely, but the detailed correlation is only fair. In the upper logged interval the poor core recovery precludes detailed comparison. The log data do, however, show considerable lithological variability, reflecting the turbiditic nature of the sediments.

Whenever possible, log runs included the Lamont Temperature Tool (LTT) for recording the borehole temperature profile. Despite the drilling disturbance, these data can provide useful constraints on equilibrium thermal profiles, and particularly on fluid flow. The data are discussed in the section on heat flow below.

The success rate of instrumental downhole measurements was not high. Even after repeated efforts with the rotatable packer no useful data were obtained, and the ONDO (ODP Nankai Downhole Observatory, temperature string) temperature tool was not successfully deployed on Leg 131. After some mechanical modification, the ONDO tool was successfully deployed on Leg 132, but as yet no measurements have been recovered from it. A Vertical Seismic Profile (VSP) experiment was limited by hole stability to the depth range 0 to 620 mbsf, and despite a high noise level, detailed processing is expected to recover a useful velocity profile from these measurements. The Lateral Stress Tool (LAST), which has been newly developed for the ODP was deployed seven times, recording data correctly on two runs. However, owing to the loss of the nonmagnetic drill collar the stress data cannot be orientated. Initial data nevertheless indicate high lateral stress and excess pore pressure at a shallow level in the accretionary prism, above 200 mbsf. The water sampling, temperature and pore pressure tool (WSTP) was run several times in various holes within the depth range 0 to 390 mbsf.

8. Heat flow

Temperature measurements were made using the WSTP tool, providing six reliable measurements in the depth range 40 to 360 mbsf (Fig. 8). These values do not fall on a simple straight line, but are fit by a regression line giving a temperature gradient of 111°C/km. Thermal conductivity data are not very tightly constrained due to poor core recovery and sediment disturbance in this interval. Nevertheless a heat flow value of 126–129 mW/m^2 can be derived. Further thermal data from the downhole logs are quite compatible with this gradient, allowing for the complex effects of drilling circulation on the borehole thermal profile. The final temperature–depth prediction for the total depth range at Site 808 is shown on Fig. 8.

The heat flow value obtained is high, but within the range of that predicted purely from conductive heat transfer from oceanic crust of this age

(125–136 mW/m^2). It is possible that a lower predicted heat flow value should be considered to allow for the effect of the very high sedimentation rate in this area. In this case the measured heat flow would suggest excess conductive flow of the same magnitude as the sedimentation rate correction.

None of the data reported here provide evidence for present-day fluid flow activity at this site. The WSTP measurement at 299 mbsf could enable us to infer a 3–4°C negative anomaly at this depth, but experimental error in this value cannot be excluded.

9. Discussion

The striking change in style of deformation and physical properties above and below the decollement is the most important finding of this leg. Comparison of Site 808 sediment porosities with several consolidation curves of marine clastic sediment and with Site 582 indicates that the accreted sediment at Site 808 is probably overconsolidated and underthrust sediment is underconsolidated. The underconsolidation and undrained condition of the underthrust sediment may be maintained by low matrix permeability and excess pore pressure.

It has been pointed out [33] that maximum pore pressure is most likely to develop in the middle of a unit of uniform, low permeability. Although this general inference can be applied to the hemipelagic sequence of Nankai prism, the question of lithological control on the particular horizon is unresolved.

The relatively coherent material from the decollement shows low porosity values (less than 30%) and conjugate faults that record NW–SE shortening. For about 100 m above the decollement there is a concentration of faults that decreases upward. Therefore, the physical properties are heterogeneous in the decollement zone and the deformation is quite asymmetrical.

Two questions arise:

(1) How can the stress regime be so different on either side of such a narrow zone?

(2) How is the porosity difference maintained?

These two issues may be inter-related. A simple assumption is that the decollement is a zone of lowest strength. If this is correct, the strength of the material at this depth must be controlled by pore pressure because no variation in lithology has been identified. This leads to a view of the decollement as a zone of highest pore pressure. Such high pore pressure would prevent upward dewatering of the underlying sediments, and produce the observed porosity changes. This in turn requires a mechanism to produce and sustain such elevated pore pressure.

The development of scaly fabrics and numerous fractures promotes the passage of fluid, and on this basis the zone should exhibit higher permeability than the hemipelagite above and below. If there is high fracture permeability, fluid flow would be required to maintain the excess pore pressure. In the absence of direct measurements of the effective pore pressure or permeability of the decollement zone, these questions can only be addressed in terms of the evidence for fluid flow along and away from the decollement.

Pore fluid geochemical data show a broad minimum in the chloride concentration profile extending from 560 to 1200 mbsf, the exact minimum lying 150 m below the decollement. As chloride is a conservative component, this dilution could be considered as a consequence of addition of low-chloride fluid to the system. Preliminary calculations of diffusion yield a rough estimate that any injection occurred several hundred thousand years ago. If the chloride signal is the evidence for large fluid flux at the decollement, why do none of the other major chemical species analysed as yet show a similar signature at or near the decollement? Further work on trace elements and isotopic ratio profiles is in progress. The Leg 131 shipboard results strongly suggest an overpressured decollement, while the nature of the fluid flow regime which sustains this remains uncertain.

Pervasive upward flow throughout the prism will affect numerous measurable parameters including heat flow and pore-water geochemistry. The thermal measurements at this site define raw thermal gradient and heat flow values which are compatible with purely conductive heat transfer from the oceanic crust. This does not preclude some component of convective transfer, perhaps compensated by the effect of very high sedimentation rates. Nevertheless, the heat flow data from Site 808 do not support any large-scale channelized flow in the accreted section.

The geochemical data provide no clear evidence for pervasive fluid flow, while at the same time failing to completely exclude the possibility of such flow. For example, the Cl gradient can be attributed, at least in part, to *in-situ* clay diagenesis. The correspondence of pore fluid geochemistry to lithological boundaries argues that any flow must be slow, most geochemical gradients being determined by reaction and diffusion.

In the light of all the evidence, we conclude that the most likely dominant mechanism for fluid expulsion from the accreted sediments at this site is upward diffusive flow through a large portion of the prism.

10. Summary and conclusions

We list below the main results of this work, some of which are illustrated in Fig. 9.

(1) Excellent correlation of seismic reflection images with lithologies, structures and physical properties of cores provided a firm foundation for interpretation of the seismic profiles.

(2) Structural geology shows considerable evidence of NW–SE shortening above the decollement and virtually no deformation below. The NW–SE shortening direction obtained from small-scale structural features coincides exactly with the seismically deduced plate convergence vector; this provided a firm base for interpreting the small-scale structures in terms of a plate tectonic context, especially in ancient rocks.

(3) Among the prominent structural features, shear bands are confined to the upper 600 m and seem to have formed earlier than the small faults.

(3a) We conclude that the stress field throughout the prism comprises a maximum horizontal compressive stress oriented NW–SE. Below the decollement the maximum principal stress is vertical. Thus the decollement acts as a zone of very low strength isolating the different stress regimes.

(4) Physical properties analysis indicates three main zones of property changes, these being above, within and below the decollement.

(4a) Sediments within the decollement are overconsolidated, and underlying subducted sediments are underconsolidated relative to their lithological equivalents above the decollement. We interpret the decollement as being overpressured.

(5) Pore pressure and *in-situ* stress was only measured in the uppermost off-scraped sediments, but preliminary results indicate that excess

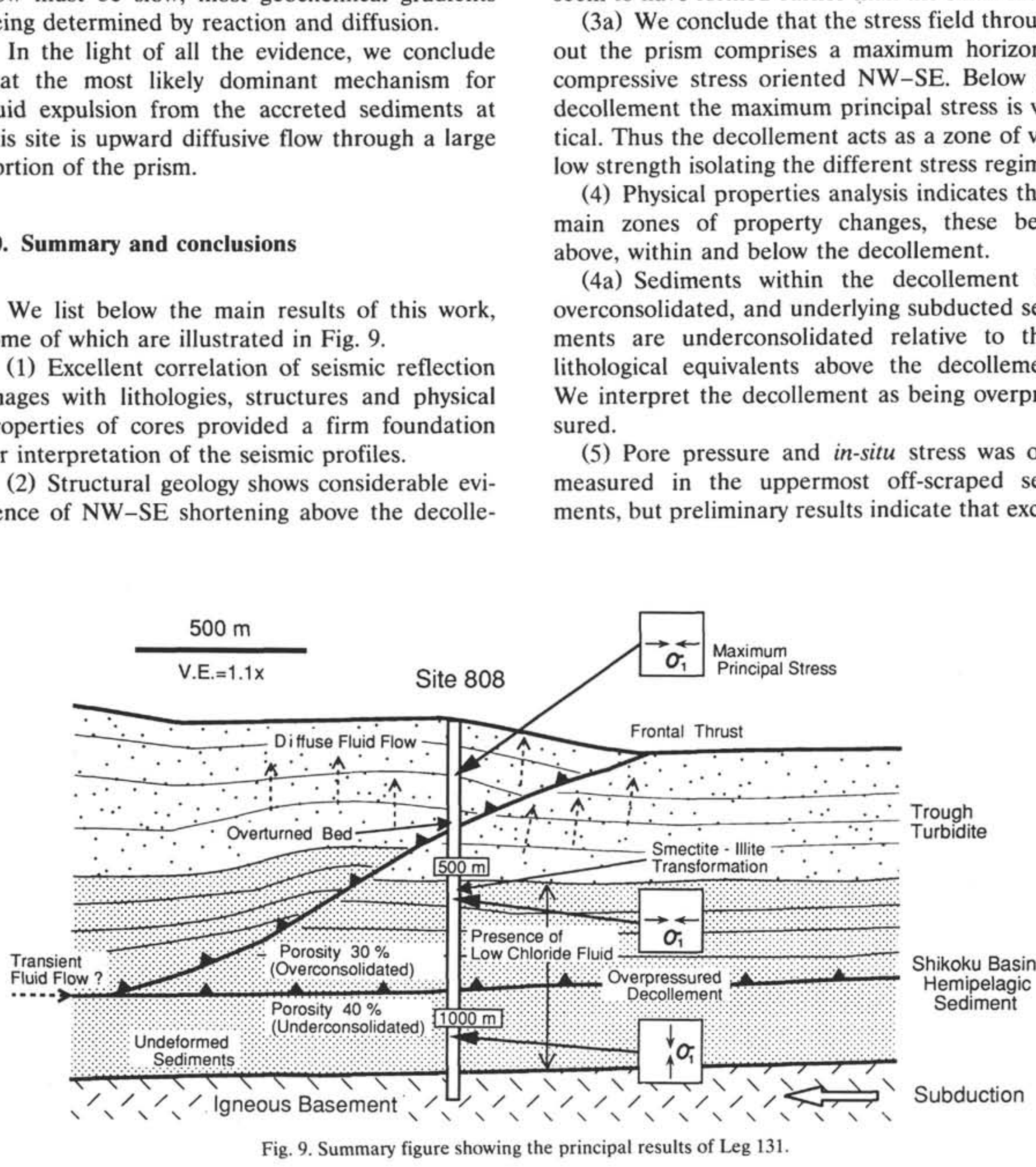

Fig. 9. Summary figure showing the principal results of Leg 131.

pore pressures and high lateral stress are found even at these relatively shallow depths.

(6) The inorganic geochemistry of the pore fluids suggests that there are four important processes operating in this prism: (1) near-surface decomposition of organic materials, (2) diagenetic effects (and possibly gas-hydrate generation), (3) equilibrium to lithological compositions, and (4) possible fluid injection. A broad Cl minimum in the lower part of the section may indicate a possible fluid injection along the decollement. However, the great width of this feature is surprising. It may have been generated, at least in part, by the dehydration reactions of clay minerals.

(7) Organic geochemistry indicates two different stratigraphic horizons of thermal generation of hydrocarbons, at 600–800 m and at 1050–1200 mbsf.

(8) The heat flow at this site is compatible with purely conductive heat transfer from the oceanic crust below.

(9) We conclude that the most likely dominant mechanism for fluid expulsion from the accreted sediments at this site is upward diffusive flow through a large portion of the prism.

Acknowledgements

The Ocean Drilling Programme Leg 131 Scientific Party thanks Captain Tom Ribbens, officers and crew of the *JOIDES Resolution*, Jack Tarbutton, the drilling superintendent, and his drilling crew, Glen Foss and Tom Pettigrew, the ODP operation superintendents, and the ODP scientific technicians for their support and cooperation. The assistance provided by J. Ashi of ORI for manuscript preparation is appreciated. Constructive comments for improvement of the manuscript by J.C. Moore and an anonymous reviewer are acknowledged.

References

1 J.C. Moore, A. Mascle, E. Taylor, P. Andreiff, F. Alvarez, R. Barnes, C. Beck, J. Behrmann, G. Blanc, K. Brown, M. Clark, J. Dolan, A. Fischer, J. Gieskes, M. Hounslow, P. McClellan, K. Moran, Y. Ogawa, T. Sakai, J. Schoonmaker, P. Vrolijk, R. Wilkens and C. Williams, Tectonics and hydrogeology of the northern Barbados Ridge: results from ODP Leg 110, Geol. Soc. Am. Bull. 100, 1578–1593, 1988.

2 N. Nasu et al., Multi-channel seismic reflection data across Nankai Trough, IPOD-Japan Basic Data Series, No. 4, 34 pp., Ocean Res. Inst., Univ. Tokyo, 1982.

3 Y. Aoki, T. Tamano and S. Kato, Detailed structure of the Nankai Trough from migrated seismic sections, in: Studies in Continental Margin Geology, J. Watkins and C.L. Drake, eds., Am. Assoc. Pet. Geol. Mem. 34, 309–322, 1982.

4 S. Kato, T. Sato and M. Sakuri, Multi-channel seismic reflection survey in the Nankai, Suruga and Sagami Troughs, Rep. Hydrogr. Res. 18, 1–23, 1983.

5 G.F. Moore, T.H. Shipley, P.L. Stoffa, D.E. Karig, A. Taira, S. Kuramoto, H. Tokuyama and K. Suyehiro, Structure of the Nankai Trough accretionary zone from multichannel seismic reflection data, J. Geophys. Res. 93, 8753–8765, 1990.

6 P.L. Stoffa, W.T. Wood, T.H. Shipley, G.F. Moore, E. Nishiyama, M.A.B. Botelho, A. Taira, H. Tokuyama and K. Suyehiro, Deep water high resolution expanding spread and split-spread marine seismic profiles in the Nankai Trough, J. Geophys. Res., in press.

7 A. Taira, J. Katto, M. Tashiro, M. Okamura and K. Kodama, The Shimanto Belt in Shikoku, Japan—evolution of Cretaceous to Miocene accretionary prism, Mod. Geol. 12, 5–46, 1988.

8 J.K. Leggett, W.S. McKerrow and D.M. Casey, The anatomy of a Lower Paleozoic accretionary forearc: the Southern Uplands of Scotland, in: Trench–Forearc Geology, J.K. Leggett, ed., Geol. Soc. London Spec. Publ. 10, 496–520, 1982.

9 K. Shiono, Seismicity of the SW Japan arc—subduction of the young Shikoku Basin, Mod. Geol. 12, 449–464, 1988.

10 N. Niitsuma, Neogene tectonic evolution of Southwestern Japan, Mod. Geol. 12, 497–532, 1988.

11 A. Taira, H. Tokuyama and W. Soh, Accretion tectonics and evolution of Japan, in: The Evolution of the Pacific Ocean Margins, Z. Ben-Avraham, ed., pp. 100–123, Oxford University Press, Oxford, 1989.

12 H. Kinoshita and M. Yamano, The heat flow anomaly in the Nankai Trough area, Init. Rep. DSDP 87, 737–743, 1986.

13 K. Kobayashi and M. Nakada, Magnetic anomalies and tectonic evolution of the Shikoku inter-arc basin, J. Phys. Earth 26, 391–402, 1978.

14 T.C. Shih, Magnetic lineations in the Shikoku Basin, Init. Rep. DSDP 58, 783–788, 1980.

15 N. Chamot-Rooke, V. Renard and X. Le Pichon, Magnetic anomalies in the Shikoku Basin: a new interpretation, Earth Planet. Sci. Lett. 83, 214–228, 1987.

16 D.M. Curtis, J. Echols et al., Lithofacies at the Shikoku and Parece Vela Basins, Init. Rep. DSDP 58, 701–710, 1980.

17 X. Le Pichon, T. Iiyama, H. Chamley, J. Charvet, M. Faure, H. Fujimoto, T. Furuta, Y. Ida, H. Kagami, S. Lallemant, J. Leggett, A. Murata, H. Okada, C. Ramgin, V. Renard, A. Taira and H. Tokuyama, Nankai Trough and fossil Shikoku Ridge: results of Box 6 Kaiko Survey, Earth Planet. Sci. Lett. 83, 186–198, 1987a.

18 X. Le Pichon, T. Iiyama, J. Boulègue, J. Charvet, M. Faure, K. Kano, S. Lallemant, H. Okada, C. Rangin, A. Taira, T. Urabe and S. Uyeda, Nankai trough and Zenisu Ridge: a deep-sea submersible survey. Earth Planet. Sci. Lett. 83, 285–299, 1987b.
19 A. Taira and N. Niitsuma, Turbidite sedimentation in the Nankai Trough as interpreted from magnetic fabric, grain size, and detrital modal analyses, Init. Rep. DSDP 87, 611–632, 1986.
20 T. Seno, The instantaneous rotation of the Philippine Sea plate relative to the Eurasian plate, Tectonophysics 42, 209–226, 1977.
21 D.E. Karig and C.L. Angevine, Geologic constraints on subduction rates in the Nankai Trough, Init. Rep. DSDP 87, 789–796, 1986.
22 Y. Aoki, H. Kinoshita and H. Kagami, Evidence of a low-velocity layer beneath the accretionary prism of the Nankai Trough: inference from a synthetic sonic log, Init. Rep. DSDP 87, 727–735, 1986.
23 M. Yamano, S. Uyeda, Y. Aoki and T.H. Shipley, Estimates of heat flow derived from gas hydrates, Geology 10, 339–343, 1982.
24 R.D. Hyndman and E.E. Davis, A mechanism for the formation of methane hydrate and sea floor bottom simulating reflectors by vertical fluid expulsion, J. Geophys. Res., in press.
25 J.C. Ingle, D.E. Karig et al., Init. Rep. DSDP 31, 1975.
26 H. Kagami, D.E. Karig, W. Coulbourn et al., Init. Rep. DSDP 87, 1986.
27 A. Taira, I.A. Hill, J. Firth et al., Proc. ODP, Init. Rep. 131, 1991.
28 H. Chamley, J.P. Cadet and J. Charvet, Nankai Trough and Japan Trench: Late Cenozoic paleoenvironments deduced from clay mineralogy data, Init. Rep. DSDP 87, 633–642, 1986.
29 D.E. Karig and N. Lundberg, Deformation bands from the toe of the Nankai accretionary prism, J. Geophys. Res. 95, 9099–9109, 1990.
30 C.J. Bray and D.E. Karig, Porosity of sediments in accretionary prisms and some implications for dewatering processes, J. Geophys. Res. 90, 768–778, 1985.
31 J.M. Gieskes, H. Elderfield and B. Nevsky, Interstitial water studies, Leg 65, Init. Rep. DSDP 65, 441–449, 1983.
32 J.M. Gieskes, P. Vrolijk and G. Blanc, Hydrogeochemistry of the Northern Barbados Accretionary Complex Transect: ODP Leg 110, J. Geophys. Res. 95, 8809–8818, 1990.
33 Y. Shi and C. Wang, Generation of high pore pressure in accretionary prisms: inferences from the Barbados subduction complex, J. Geophys. Res. 93, 8893–8910, 1988.